

Rainbow correlation imaging with macroscopic twin beam

This content has been downloaded from IOPscience. Please scroll down to see the full text.

2017 J. Opt. 19 064001

(<http://iopscience.iop.org/2040-8986/19/6/064001>)

View [the table of contents for this issue](#), or go to the [journal homepage](#) for more

Download details:

IP Address: 193.206.161.84

This content was downloaded on 15/05/2017 at 09:19

Please note that [terms and conditions apply](#).

You may also be interested in:

[Orbital angular momentum modes of high-gain parametric down-conversion](#)

Lina Beltran, Gaetano Frascella, Angela M Perez et al.

[Interference of macroscopic beams on a beam splitter: phase uncertainty converted into photon-number uncertainty](#)

K Yu Spasibko, F Töppel, T Sh Iskhakov et al.

[Spectral ensemble ghost imaging](#)

Nandan Jha

[Direct generation of genuine single-longitudinal-mode narrowband photon pairs](#)

Kai-Hong Luo, Harald Herrmann, Stephan Krapick et al.

[A characterization of the single-photon sensitivity of an electron multiplying CCD](#)

Lijian Zhang, Leonardo Neves, Jeff S Lundeen et al.

[Coherence and mode decomposition of weak twin beams](#)

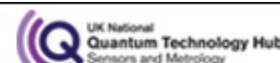
Jan Peina Jr

[Macroscopic Hong–Ou–Mandel interference](#)

T Sh Iskhakov, K Yu Spasibko, M V Chekhova et al.

brightrecruits
WEBINAR

Studentship opportunities with the UK's
National Quantum Technology Hubs



Rainbow correlation imaging with macroscopic twin beam

Alessia Allevi^{1,2} and Maria Bondani²

¹Dipartimento di Scienza e Alta Tecnologia, Università degli Studi dell'Insubria, Via Valleggio 11, I-22100 Como, Italy

²Istituto di Fotonica e Nanotecnologie, Consiglio Nazionale delle Ricerche, Via Valleggio 11, I-22100 Como, Italy

E-mail: maria.bondani@uninsubria.it

Received 6 December 2016, revised 20 March 2017

Accepted for publication 11 April 2017

Published 5 May 2017



CrossMark

Abstract

We present the implementation of a correlation-imaging protocol that exploits both the spatial and spectral correlations of macroscopic twin-beam states generated by parametric downconversion. In particular, the spectral resolution of an imaging spectrometer coupled to an EMCCD camera is used in a proof-of-principle experiment to encrypt and decrypt a simple code to be transmitted between two parties. In order to optimize the trade-off between visibility and resolution, we provide the characterization of the correlation images as a function of the spatio-spectral properties of twin beams generated at different pump power values.

Keywords: parametric downconversion, photon statistics, spatio-spectral coherence in twin beam, correlation imaging

(Some figures may appear in colour only in the online journal)

1. Introduction

Over the past 30 years, the twin-beam (TWB) states produced by the nonlinear process of spontaneous parametric downconversion (PDC) have been widely used to realize correlation imaging protocols both at single-photon level [1–3] and in the macroscopic domain [4]. Actually, the implementation of such protocols does not require the light to be entangled, but only the existence of photon-number correlations between the parties of a bipartite state [5–7]. That is why also classically correlated optical states can be used to perform imaging protocols. Typically, an object is placed in one arm of the correlated light and an image, the ‘ghost image’, is reconstructed by the light in the other arm, which never interacted with the object. The ghost-imaging technique was proposed by Klyshko in the late 80s [8, 9] as a peculiar application of PDC light at single-photon level. According to the original scheme, the photons of a pair are sent to two different imaging systems: the signal illuminates an object and is then detected by a ‘bucket’ detector, whereas the idler is revealed by a detector endowed with spatial resolution. Information about the object is obtained from the coincidences of signal-idler photon pairs as a function of the transverse position of

the detector in the idler arm [10]. Since then, several protocols have been demonstrated in different intensity regimes [3–5] and also with different kinds of correlated-light sources [11–15]. Moreover, the performance of the protocol in terms of visibility, resolution and signal-to-noise ratio have been investigated, both theoretically and experimentally, at different correlation orders [4, 16–19].

A substantial advance in the applicability of ghost-imaging protocols has been achieved thanks to the use of spatial light modulators [20–22], which allow the deterministic preparation of the light to be used. Recently, the use of polychromatic light has also been introduced to obtain colored images [23] or to improve the quality of the ghost images [24].

In the case of polychromatic TWB states, the existence of spectral correlations represents an additional resource for the implementation of ghost-imaging protocols, which usually exploit the spatial correlations between signal and idler arms. In this paper we use the results of recent investigations, in which the spatial and spectral properties of TWB states have been studied at different PDC gains up to pump depletion [25], to show how the pump power can influence the parameters usually involved in imaging protocols, namely the

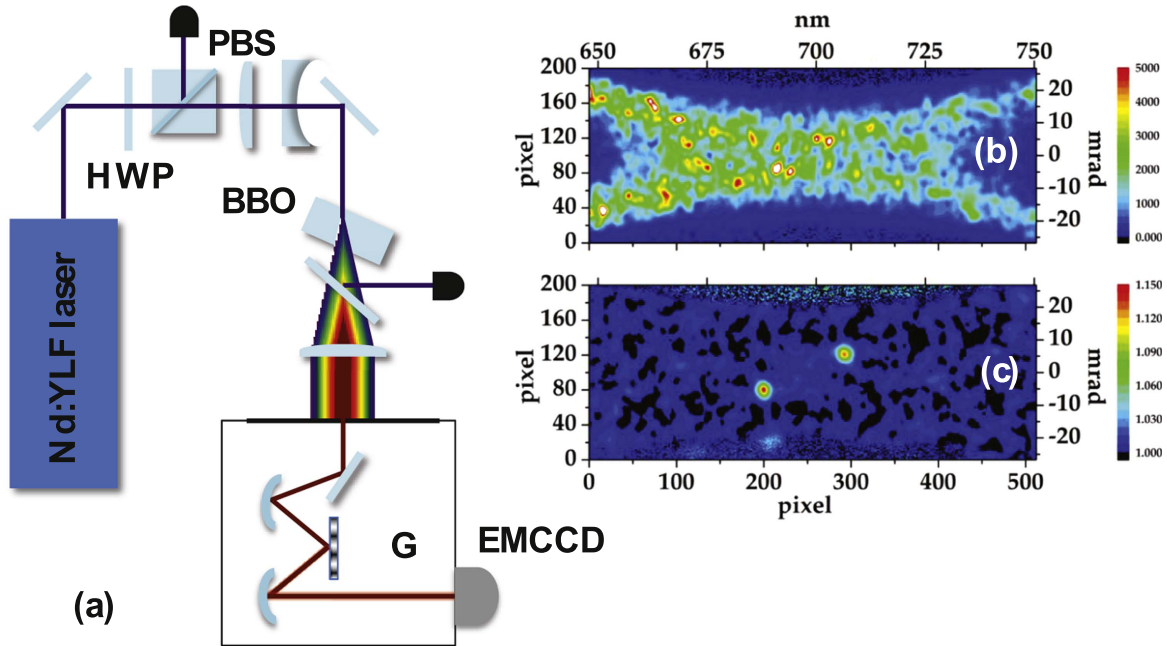


Figure 1. (a) Sketch of the experimental setup. HWP: half-wave plate; PBS: polarizing cube beam splitter; BBO: nonlinear crystal; G: grating; EMCCD: electron-multiplying CCD camera. (b) Single-shot image exhibiting the typical X-wave pattern. (c) Typical example of correlation matrix, C , in which the autocorrelation area is on the left side of the image and the cross-correlation area on the right side. For a better comparison, in panels (b) and (c) the horizontal and vertical axes are expressed in pixel units as well as in nanometers and milliradians, respectively.

visibility and the spatial resolution, and we discuss how to optimize the trade-off between these two quantities. Moreover, we also investigate the possibility to exploit the spectral resolution that characterizes our detection system to realize novel correlation imaging protocols. In particular, we propose a proof-of-principle experiment, in which the spectral properties of TWB states represent the crucial resource both to encrypt and decrypt a simple code to be transmitted between the two parties. The resolution exploited in the proof-of-principle experiment is also achievable with the current technology of high-transmissivity bandpass filters.

2. Methods

The experimental setup is sketched in figure 1(a). The third-harmonic pulses (349 nm, 4.5 ps pulse duration) of a mode-locked Nd:YLF laser regeneratively amplified at 500 Hz (High-Q-Laser) are sent to a type-I 8 mm long β -barium borate crystal (cut angle = 37°) to produce TWB states from PDC. A half-wave plate followed by a polarizing cube beam splitter, both placed in front of the crystal, are used to vary the pump mean power and hence to change the gain of the PDC process. A portion of the downconverted light, generated close to frequency degeneracy and in a slightly non-collinear configuration geometry, is collected by a 60 mm focal length lens and focused on the plane of the vertical slit of an imaging spectrometer (Lot Oriel), equipped with a $600 \text{ lines mm}^{-1}$ grating. The angularly dispersed far-field radiation is then recorded shot-by-shot by a synchronized EMCCD camera (iXon Ultra 897, Andor), operated at full frame resolution

(512×512 pixels, $16 \mu\text{m}$ pixel size) both in the presence and in the absence of the electron-multiplying gain. The resulting resolution of the system composed of the imaging spectrometer and the EMCCD camera is 0.2 nm in spectrum and 0.015° in angle. In figure 1(b), we show a typical single-shot image, in which the X-wave shape of the speckle-like pattern is clearly evident. In the picture the horizontal axis refers to spectrum, whereas the vertical axis gives information about the angular dispersion of the radial direction of PDC light. Note that the existence of intensity correlations between different portions of the pattern is testified by the presence of spatio-spectral coherence areas symmetric with respect to the degenerate wavelength and the collinear direction, which correspond to the center of the image. Even if the geometry of the system does not implement any true imaging scheme, it is anyway useful for investigating the role of the different parameters involved in the generation of PDC light on the quality of correlation-imaging protocols. Indeed, as recently shown in [25], the size of spatio-spectral coherence areas as well as the number of modes inside a single area exhibit a non-trivial dependence on pump power due to the occurrence of pump depletion. Such properties can be investigated by calculating the intensity correlation coefficient between a single pixel (i, j) and all the pixels contained in a single-shot image, namely

$$C_{k,l}^{(i,j)} = \frac{\langle I_{i,j} I_{k,l} \rangle}{\langle I_{i,j} \rangle \langle I_{k,l} \rangle}, \quad (1)$$

where $I_{k,l}$ is the intensity value of each pixel expressed in digital numbers, upon subtraction of the mean value of the noise measured with the camera in perfect dark, and $\langle \dots \rangle$

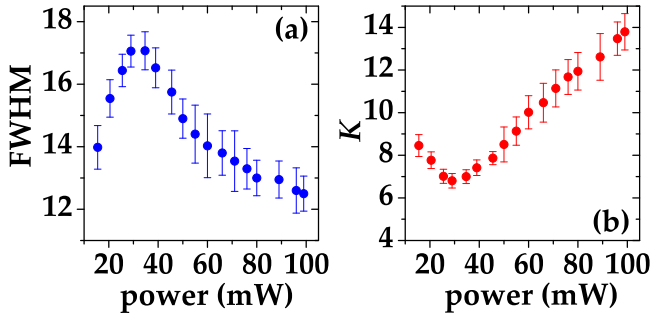


Figure 2. (a) Spatial FWHM width, expressed in pixel units, of the cross-correlation areas as a function of the pump mean power. (b) Number of modes K , contained in a single pixel, as a function of pump mean power. In both panels the error bars were obtained by applying the calculation of C to several input pixels.

indicates the averaging over a sequence of 1000 subsequent images. Note that the definition in equation (1) is independent of the gain of the camera and hence does not require any calibration procedure. Actually, the function $C_{k,l}^{(i,j)}$ defined in equation (1) is a matrix having the same size as the original images and containing both the intensity auto and the cross-correlation areas (see figure 1(c)).

In view of imaging applications, we remark that the vertical full-width at half maximum (FWHM) width of the cross-correlation areas sets the spatial resolution of the system [4, 11].

As shown in figure 2(a), the evolution of the spatial FWHM width as a function of the pump mean power displays an initial growth of the spatial width followed by a decrease at increasing pump powers. The maximum value of the FWHM width corresponds to the onset of pump depletion. The same behavior can be observed in the evolution of the spectral FWHM width [25]. This evolution suggests that the best resolution, corresponding to the smallest area size, can be achieved at low as well as at high pump power values.

On the contrary, in imaging protocols also the visibility of the images is a crucial parameter to be investigated. As this quantity is essentially increasing at decreasing values of the number of modes K inside a spatio-spectral area, the smaller the number of modes the larger the corresponding visibility value [19]. In figure 2(b) we show the number of modes calculated from the maximum value $g^{(2)} \equiv C_{i,j}^{(i,j)}$ of the auto-correlation areas according to the relation $K = 1/(g^{(2)} - 1)$ [26–28], as already explained in [25]. We notice that the value of K as a function of the pump mean power is complementary to that of the size of spatio-spectral coherence areas, so that the minimum number of modes corresponds to the maximum value of the spatial FWHM width: this outlines the expected trade-off between visibility and resolution.

3. Results and discussion

In order to explore the usefulness of the system described so far for imaging applications, we consider a simple toy model: on the left side of each single-shot image we select a group of pixels as the object [29]. This corresponds to locating a mask

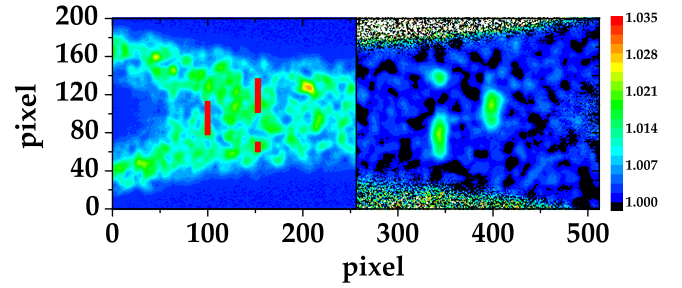


Figure 3. Left side: single-shot image to which the object (see the red rectangles) we want to reconstruct is superimposed. Right side: portion of the correlation imaging C containing the transparency of the object. Note that the column bar refers only to the panel on the right-hand side.

in the plane of the camera sensor. As a typical example, on the left side of figure 3 we show a single-shot X-wave image containing a mask chosen as the object. The mask is located in the left part of the X-wave (the signal). The mask is composed of three elements (see the red rectangles) occupying different spatial positions and characterized by a defined spectral width (5 px–1 nm). By analogy with conventional ghost-imaging protocols, we then consider a bucket detector, by summing all the intensity values in the mask. The values of the bucket are used to evaluate the correlation with the intensity of all the pixels of the same image according to equation (1). On the right side of figure 3 we plot the right portion (the idler) of the obtained correlation matrix C . The correlation was averaged over 1000 consecutive single-shot images. Note that even if in the region of the idler there is no direct image of the object, nevertheless, the correlation reconstructs the mask selected in the signal. Since in the idler beam there is no imaging system, which would be required by the traditional ghost-imaging protocol, the correlation reproduces the shape of the mask more like a ‘shadow’ than an image. Hereafter, we will refer to this ‘shadow’ as the transparency of the object [30].

Though not being a true ghost-imaging scheme, our system is still interesting for imaging applications as it allows the investigation of the effects of spectral resolution that are not easily accessible with standard imaging schemes.

To start with the characterization of the system, we discuss the results of our correlation imaging scheme as a function of pump power. As the object, we choose a triple slit occupying 115 pixels, i.e. 1.84 mm, (including the free space between the elements of the slit) in the spatial direction and 5 pixels in the spectral direction. In figure 4 we show the contour plots of the corresponding correlation matrices for three different pump mean power values. In each panel, it is possible to recognize the presence of a structure representing the transparency of the chosen object. We notice that in the horizontal direction the FWHM width of the image is definitely larger than the object size. This feature testifies that the transparency of the object is actually obtained by the convolution of the object width with the spectral width of the coherence areas [31]. In the spectral direction such a value is roughly 15 pixels, to be compared with the spectral transmittance of the object (5 pixels). On the contrary, in the

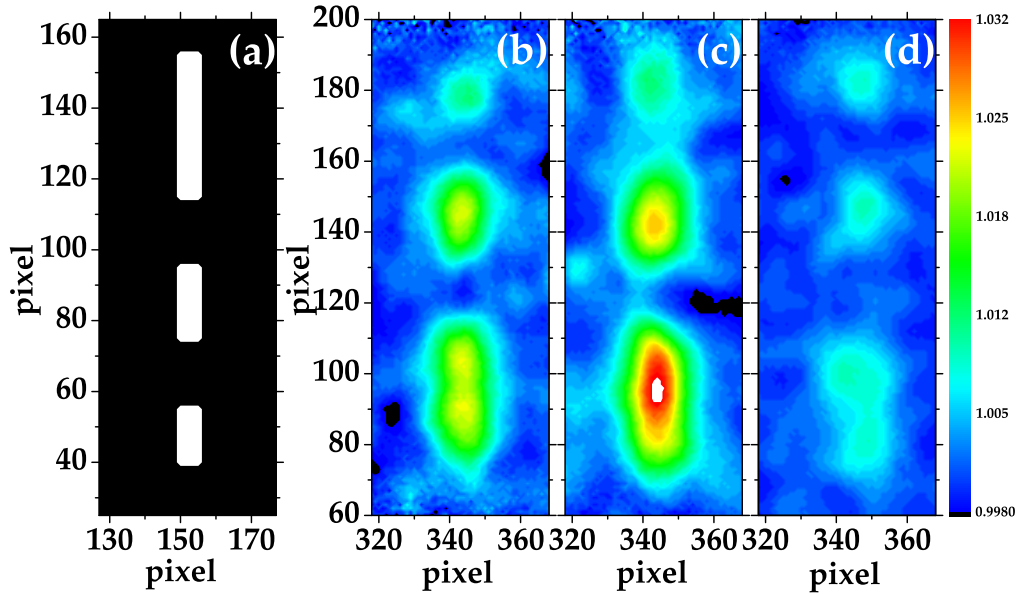


Figure 4. (a) Theoretical image of the triple slit used as the object. (b)–(d) Contour plots of the portions of C containing the transparency of the triple-slit object. The panels correspond to different choices of pump mean power. Panel (b) $P = 20.5$ mW; panel (c) 34.7 mW; panel (d) 60 mW. Panel (c) corresponds to the power at which pump depletion occurs. For a better comparison, the intensity levels are the same in all panels.

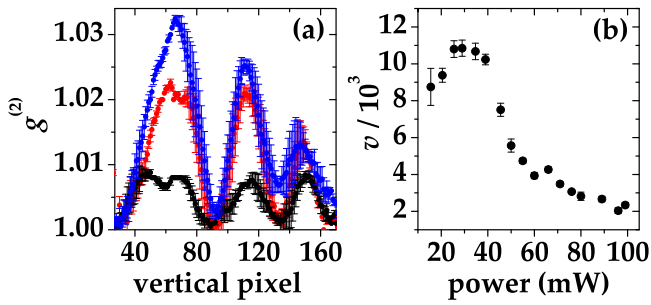


Figure 5. (a) Vertical sections of the images shown in figure 4 and taken around the maximum value of the portion of C containing the transparency of the object. The red curve corresponds to panel (b), the blue curve to panel (c), and the black curve to panel (d). (b) Visibility v of the images as a function of the pump mean power.

spatial direction the size of the object is almost reproduced, in agreement with the geometry of the system. To better compare the three experimental conditions of figure 4, in figure 5(a) we plot the corresponding vertical sections taken around the maximum value of C . Even if all the sections reconstruct the triple-slit, their absolute values are different. The quality of the reconstructed images can be quantified in terms of the visibility

$$v = (g_{IN}^{(2)} - g_{OUT}^{(2)}) / (g_{IN}^{(2)} + g_{OUT}^{(2)}), \quad (2)$$

where $g_{IN}^{(2)}$ is the mean value of C inside the image and $g_{OUT}^{(2)}$ is the mean value in a portion of the matrix that does not contain the image. In figure 5(b) we present the visibility of the triple-slit image as a function of pump mean power. As expected, the highest values of v are achieved at pump power values close to the occurrence of depletion, that is in the same experimental condition where the number of modes contained in a single coherence area attains its minimum value (see figure 2(b)).

However, since this experimental condition corresponds to the maximum width of the coherence areas (see figure 2(a)), in the following we will continue the investigation of our system for imaging applications at a pump power value for which the best compromise between maximum visibility and optimal resolution is achieved. This situation occurs at low pump power values, that is in the condition in which coherence areas are quite small and at the same time the internal number of modes is rather low. In particular, we choose to deal with the images taken at $P = 20.5$ mW.

In a traditional imaging system based on PDC light, the spectral resolution given by the imaging spectrometer is not easily achievable. In fact, the object is usually illuminated by a multi-mode thermal, i.e. polychromatic, light and the image obtained by applying the ghost-imaging protocol is also reconstructed by a multi-mode thermal light. However, the polychromatic nature of PDC light reduces the visibility of the resulting image, being it associated with a large number of spectral modes. As anticipated above, the spectral resolution offered by our imaging system can be employed to improve the quality of the correlation images. We again choose the triple slit described above as the object, and consider the correlation image obtained by correlating the values of the bucket with the idler at different spectral binning. In more detail, before evaluating the correlation, we bin the values of the idler in the horizontal direction (the vertical one is left unchanged) in bins of increasing width and fixed central wavelength. Each bin size corresponds to put a filter with a given spectral width in front of the detector used to reconstruct the correlation image. In figure 6 we show the sections of the correlation images at different values of the horizontal bin size (left panel) as well as the corresponding visibility values (right panel). We notice that in both panels the best results correspond to the highest spectral resolution (1 px–0.2 nm). However, it is worth noting that this

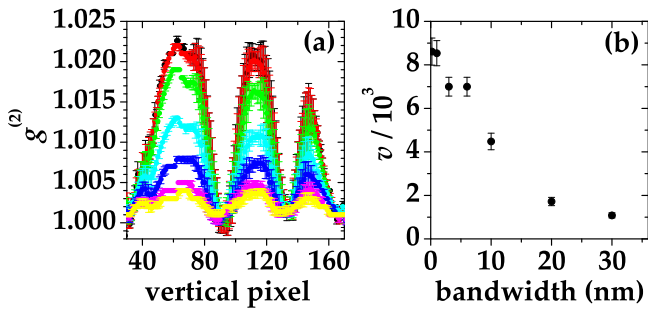


Figure 6. (a) Vertical sections of the correlation images of the triple-slit object obtained by means of different horizontal bin sizes applied to the right side of the single-shot images. The higher the value of the vertical sections the smaller the bin size. From bottom to top, the bin size is: 30, 20, 10, 6, 3, 1, 0.2 nm. (b) Visibility as a function of the bin size.

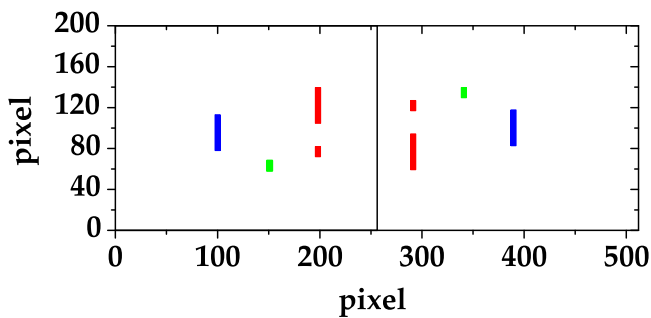


Figure 7. Sketch of the mask containing the secret code we want to transmit. The mask is placed on the left side of the X -wave, whereas the expected correlation image is reconstructed on the right side.

choice is similar to the case of 1 nm resolution. We ascribe such a similarity to the fact that the object itself has a 1 nm spectral width. On the contrary, for larger bin sizes the visibility rapidly decreases, since the coherence areas that contribute to the image reconstruction are combined with others that do not contribute to the image formation. In particular, the larger the bin size the lower the visibility.

Since the image visibility benefits from the spectral resolution offered by our system, we can exploit such a resource to encrypt and decrypt a simple code to be transmitted between two parties. As shown in figure 7, on the signal side of each single-shot image we select a mask extending on three different spectral regions of transmissivity and different spatial extensions. Let us assume that only one of the spectral regions, say the leftmost one, contains the code we want to transmit, whereas the other two contain decoy codes. Ideally, on the idler side we would expect an image in which the rightmost spectral region contains the code (see the right side of figure 7).

As a matter of fact, the experimental correlation matrices are able or not to properly decrypt the transmitted code depending on the choice of the bin size on the idler side. For instance, in panel (a) of figure 8 we show the contour plot of the correlation matrix when a single horizontal 36 nm wide bin has been imposed to the single-shot images. Such a situation corresponds to having no serious spectral filtering on

the portion of PDC light used to reconstruct the transparency of the object. In the picture the code that we want to transmit results completely indistinguishable from the rest (see the vertical section in panel (b)). Better results in the decryption of the code can be achieved by increasing the spectral resolution. In figure 8(d) the contour plot of the correlation matrix shows three 18 nm wide regions, in which only the one on the right gives information about the transmitted code. Also the vertical sections shown in panel (e) indicate that the mask used as the object is characterized by three different spectral regions of transmissivity. By further improving the spectral resolution, the results appear even clearer. In panel (g), each spectral region of the contour plot is 5.2 nm wide. The three sections in panel (h) are endowed with a visibility that is higher than the one reached in panels (b) and (e) (see the different values of $g^{(2)}$ reported on the horizontal axes). The results can be better emphasized by converting the values of $g^{(2)}$ appearing in the sections of panels (b), (e), and (h) to binary digits. In particular, in each panel we assign the logic value 0(1) to the values that are lower(higher) than half the maximum of the highest peak of the sections. In the section of panel (b), the threshold is fixed at 1.002, in the sections of panel (e) at 1.003 and in the sections of panel (h) at 1.006. The conversion in binary digits is shown in panels (c), (f) and (i), respectively. As a final remark for the implementation of the protocol, we notice that to perform the proof-of-principle scheme the only secret key that must be shared between the two parties is the central wavelength at which the correlation matrix must be calculated.

4. Conclusions

In this work, the existence of correlations in different degrees of freedom (space and spectrum) has been exploited as a resource for the implementation of a novel imaging scheme. The spatio-spectral resolution of an imaging spectrometer played a major role in the investigation of the experimental conditions in which a macroscopic TWB can be used to perform correlation-imaging protocols. In particular, we studied the evolution of the spatial resolution and of the visibility of the images at different pump mean power values. Moreover, we investigated the role of the spectral resolution in the implementation of imaging protocols. The use of a narrow spectral filtering not only enhances the visibility and thus the quality of the reconstructed correlation images, but it can be also useful to encrypt and decrypt a simple binary code to be transmitted between the two parties of TWB. Even if formally the setup used to implement these proof-of-principle experiments is not an imaging scheme, the obtained results can be extended to the already existing imaging protocols and also applied to the development of novel schemes for the transmission of secret codes. To this aim, we note that the current technology of bandpass filters is suitable to achieve the same spectral resolution exhibited by the system described in the paper.

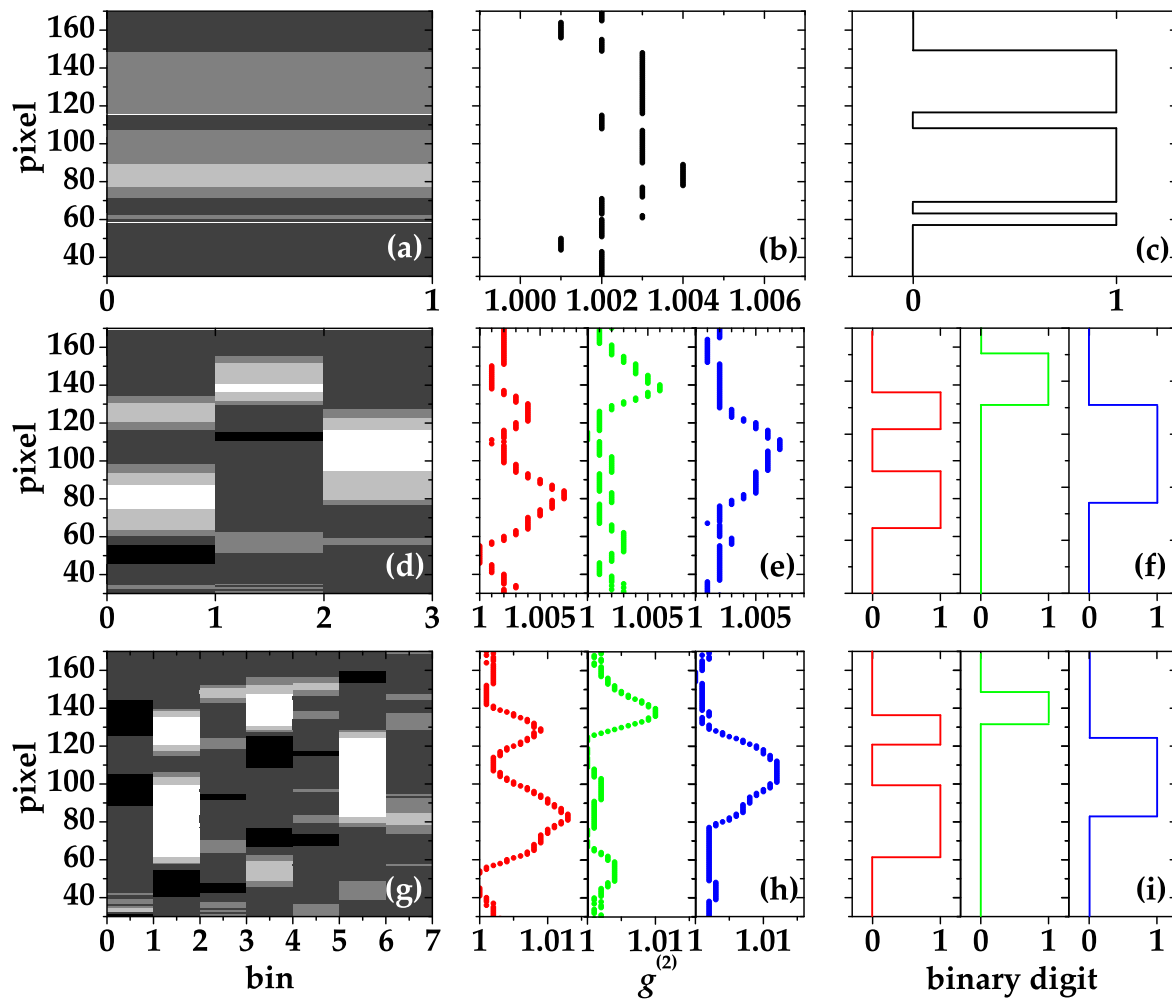


Figure 8. (a), (d) and (g) Contour plots of the portion of C containing the transparency of the mask used to send the secret code. The spectral resolution is increased from top to bottom. (b), (e) and (h) Vertical sections of the portions of the correlation images in which some information about the mask is present. (c), (f) and (i) Conversion of the vertical sections in binary digits.

References

[1] Souto Ribeiro P H, Padua S, Machado da Silva J C and Barbosa G A 1994 *Phys. Rev. A* **49** 4176–9

[2] Strekalov D V, Sergienko A V, Klyshko D N and Shih Y H 1995 *Phys. Rev. Lett.* **74** 3600–3

[3] Pittman T B, Shih Y H, Strekalov D V and Sergienko A V 1995 *Phys. Rev. A* **52** R3429–32

[4] Bondani M, Allevi A and Andreoni A 2012 *Eur. Phys. J. Spec. Top.* **203** 151–61

[5] D’Angelo M and Shih Y H 2005 *Laser Phys. Lett.* **2** 567–96

[6] Scarcelli G, Berardi V and Shih Y 2006 *Phys. Rev. Lett.* **96** 063602

[7] Gatti A, Bondani M, Lugiato L A, Paris M G A and Fabre C 2007 *Phys. Rev. Lett.* **98** 039301

[8] Klyshko D N 1988 *Zh. Eksp. Teor. Fiz* **94** 82–90

[9] Klyshko D 1988 *Photons and Nonlinear Optics* (New York: Gordon and Breach)

[10] Abouraddy A, Saleh B, Sergienko A V and Teich M 2001 *Phys. Rev. Lett.* **87** 123602

[11] Puddu E, Andreoni A, Degiovanni I P, Bondani M and Castelletto S 2007 *Opt. Lett.* **32** 1132–4

[12] Bondani M, Puddu E, Degiovanni I P and Andreoni A 2008 *J. Opt. Soc. B* **25** 1203–13

[13] Ferri F, Magatti D, Gatti A, Bache M, Brambilla E and Lugiato L A 2005 *Phys. Rev. Lett.* **94** 183602

[14] Valencia A, Scarcelli G, D’Angelo M and Shih Y H 2005 *Phys. Rev. Lett.* **94** 063601

[15] Zhang D, Zhai Y H, Wu L A and Chen X H 2005 *Opt. Lett.* **30** 2354–6

[16] Chan K W C, O’Sullivan M N and Boyd R W 2009 *Opt. Lett.* **34** 3343–5

[17] O’Sullivan M N, Chan K W C and Boyd R W 2010 *Phys. Rev. A* **82** 053803

[18] Chen X H, Agafonov I N, Luo K H, Liu Q, Xian R, Chekhova M V and Wu L A 2010 *Opt. Lett.* **35** 1166–8

[19] Iskhakov T, Allevi A, Kalashnikov D A, Sala V G, Takeuchi M, Bondani M and Chekhova M 2011 *Eur. Phys. J. Spec. Top.* **199** 127–38

[20] Shapiro J H 2008 *Phys. Rev. A* **78** 061802(R)

[21] Bromberg Y, Katz O and Silberberg Y 2009 *Phys. Rev. A* **79** 053840

[22] Sun B, Edgar M P, Bowman R, Vittert L E, Welsh S, Bowman A and Padgett M J 2013 *Science* **340** 844–7

[23] Welsh S S, Edgar M P, Bowman R, Jonathan P, Sun B and Padgett M J 2013 *Opt. Express* **21** 23068–74

[24] Duan D, Du S and Xia Y 2013 *Phys. Rev. A* **88** 053842

[25] Allevi A, Jedrkiewicz O, Brambilla E, Gatti A, Peřina J Jr., Haderka O and Bondani M 2014 *Phys. Rev. A* **90** 063812

- [26] Christ A, Laiho K, Eckstein A, Casseiro K N and Silberhorn C 2011 *New J. Phys.* **13** 033027
- [27] Pérez A M, Iskhakov T S, Sharapova P, Lemieux S, Tikhonova O V, Chekhova M V and Leuchs G 2014 *Opt. Lett.* **39** 2403–6
- [28] Sharapova P, Pérez A M, Tikhonova O V and Chekhova M V 2015 *Phys. Rev. A* **91** 043816
- [29] Brida G, Chekhova M V, Fornaro G A, Genovese M, Lopaeva E D and Ruo Berchera I 2011 *Phys. Rev. A* **83** 063807
- [30] Goodman J W 1968 *Introduction to Fourier Optics* (New York: McGraw-Hill)
- [31] Ferri F, Magatti D, Sala V G and Gatti A 2008 *Appl. Phys. Lett.* **92** 261109